Microbiome

RESEARCH Open Access

The mitigation of spatial constraint in porous environments enhances biofilm phylogenetic and functional diversity

Chengxia Fu[1], Yichao Wu[1*], Søren J. Sørensen[2], Ming Zhang[1], Ke Dai[1], Chunhui Gao[1], Chenchen Qu[1], Qiaoyun Huang[1] and Peng Cai[1]

Abstract

Background Porous environments constitute ubiquitous microbial habitats across natural, engineered, and medical settings, offering extensive internal surfaces for biofilm development. While the physical structure of the porous environment is known to shape the spatial organization of biofilm inhabitants and their interspecific interactions, its influence on biofilm community structure and functional diversity remains largely unknown. This study employed microfluidic chips with varying micropillar diameters to create distinct pore spaces that impose different levels of spatial constraints on biofilm development. The impact of pore spaces on biofilm architecture, community assembly, and metabolic functions was investigated through in situ visualization and multi-omics technologies.

Results Larger pore sizes were found to increase biofilm thickness and roughness while decreasing biofilm coverage over pore spaces. An increase in pore size resulted in reduced biofilm community evenness and increased phylogenetic diversity. Remarkably, biofilms in 300-μm pore spaces displayed the highest richness and the most complex and interconnected co-occurrence network pattern. The neutral model analysis demonstrated that biofilm assembly within different pore spaces was predominantly governed by stochastic processes, while deterministic processes became more influential as pore space increased. Exometabolomic analyses of effluents from the microfluidic chips further elucidated a significant correlation between the exometabolite profiles and biofilm community structure. The increased community richness in the 300-μm pore space was associated with the significantly higher exometabolome diversity.

Conclusions Collectively, our results indicate that increased pore space, which alleviated spatial constraints on biofilm development, resulted in the formation of thicker biofilms with enhanced phylogenetic and functional diversity.

Keywords Biofilm, Pore space, Spatial constraints, Community assembly, Microfluidics, Multi-omics

Background

Biofilm represents the predominant microbial lifestyle in natural, engineered, and medical environments [1]. Porous media, such as soil, aquifers, industrial filters, and medical stents, serve as idea habitats for biofilm colonization and inhabitation [2–4]. The sessile lifestyle confers multifaceted advantages to biofilm inhabitants, allowing them to sequester nutrients, withstand shear stress, and protect against antimicrobial agents [5]. The biofilm development, in turn, exerts profound influences on the

*Correspondence:
Yichao Wu
wuyichao@mail.hzau.edu.cn
[1] National Key Laboratory of Agricultural Microbiology, College of Resources and Environment, Huazhong Agricultural University, Wuhan 430070, China
[2] Section of Microbiology, Department of Biology, University of Copenhagen, Copenhagen, Denmark

physical and biochemical environment of porous media systems, playing a crucial role in the biogeochemical cycle, bioremediation, and chronic infection [6]. Therefore, elucidating the assembly of biofilm communities in porous environments is crucial to unveil the pivotal roles of biofilm across various ecosystems and develop novel strategies for their prevention, management, and engineering.

The physical structure of the porous environment has been identified as one key determinant in shaping microbial communities. The intricate physical architecture reduces the transport of nutrients, signal molecules, and wastes, generating microscale resource gradients to allow a wide microbial diversity via niche specialization [7]. The porous environments also enable the coexistence of weak and strong competitors by reducing competitive pressure through spatial segregation [8–10]. Niche differentiation was thus posited to drive the elevated diversity observed in small soil aggregates and fine-textured sediments [11, 12]. Meanwhile, biofilm formation serves as a competitive strategy for space and nutrient [13]. Previous studies have found that biofilm-forming species eradicate biofilm-deficient competitors via smothering them and cutting off nutrient access [14, 15]. In porous media with limited space and restricted nutrient accessibility, biofilm protrudes from the grains into the pore space to sequester nutrients and impede the colonization of other species on the grains [16]. Consequently, the intensified competition driven by biofilm formation contradicts the observed enhanced diversity in confined pore spaces, and the underlying mechanisms governing the assembly of intricate communities within porous media have yet to be fully elucidated. Moreover, the current understanding of how pore spaces influence biofilm community assembly largely depends on environmental sampling and grain size classification, which inherently confound the effects of pore spaces with other environmental variables, such as the variations in organic and mineral composition [17]. Therefore, the exclusive impact of pore spaces on biofilm assembly remains largely unexplored.

In order to address this knowledge gap, we investigated the assembly of biofilm communities and their functional features in pore spaces with different levels of spatial constraints (Fig. 1). The microfluidic chips incorporating arrays of micropillars with varying diameters were developed to simulate different porous environments. This approach allowed for the in situ monitoring of biofilm structure and morphology within the controlled pore spaces. The biofilm community compositions were revealed via 16S amplicon sequencing, and the assembly mechanisms were elucidated using the Sloan's neutral community assembly model. Exometabolomic

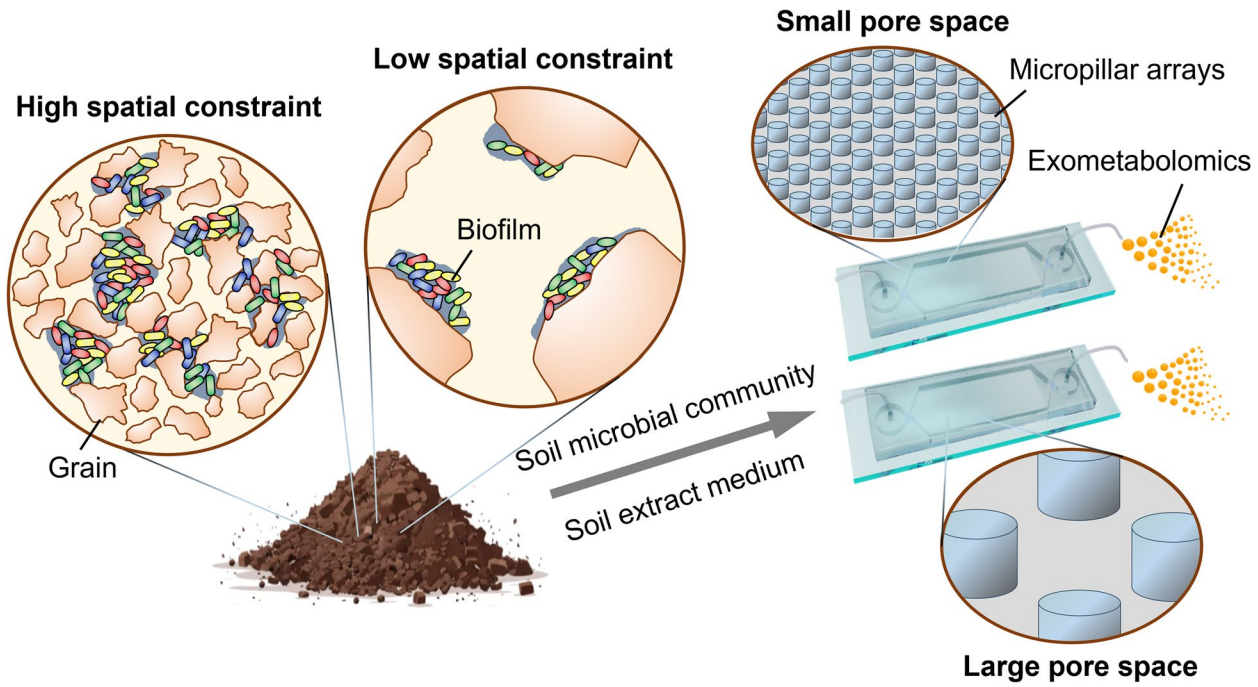

Fig. 1 Microfluidic platform to study soil biofilm assembly and function under varying spatial constraints. The microfluidic chips contain micropillars of different diameters to impose varying levels of spatial constraints on biofilm development. A soil microbial community extracted from woodland topsoil was cultivated in the microfluidic devices using a soil extract medium prepared from the same soil sample. Biofilm functional characteristics were analyzed through exometabolomic profiling of the effluent from the microfluidic chips

analyses were further employed to provide insights into the functional properties of biofilms in different pore spaces. Our study highlights how expanded pore spaces drive the assembly of phylogenetically distant biofilm communities.

Results

Reduced spatial constraints promoted biofilm formation

To investigate the influence of pore space on biofilm assembly, we fabricated the microfluidic chips with micropillar arrays featuring distinct diameters and spacings at dimensions relevant to biofilm. Given that biofilms were generally tens of micrometers thick, pore sizes of 20, 50, 100, and 300 μm were chosen to impose different levels of spatial constraints (Supplementary Fig. S1). The longitudinal section areas were kept the same across different chips, and the height of flow channels matched the corresponding micropillar diameter. This configuration ensures a uniform porosity of 0.77 for all chips. To initiate biofilm development in the porous media, soil microbial communities were inoculated into the microfluidic devices and cultured using the intensive soil extract medium (ISEM) prepared from the same soil sample (Supplementary Fig. S2). Due to the varying volumes of the microfluidic chambers with different pore sizes, the fresh medium was introduced at a flow rate proportional to each chamber's volume. This approach ensured that the fresh medium remained in the flow chambers for an identical duration, subjecting the biofilms to the same flow velocity and shear force.

Biofilms in different pore spaces originated from the small colonies on the micropillar surface and displayed distinct morphologies upon maturation (Fig. 2a & Supplementary Fig. S3). Microscopic image analysis was performed to quantify key biofilm characteristics: thickness (radial distance from biofilm edges to the micropillar surface), roughness (standard deviation of thickness on individual micropillars), and coverage (proportion of pore space occupied by biofilms) (Fig. 2b). Greater biofilm roughness and thickness were observed in larger pore spaces with reduced spatial constraints (Fig. 2c). In the pore sizes ranging from 20 to 100 μm, the biofilms extruded from the micropillar surface into the fluid to form streamer-like structures, which contributed to

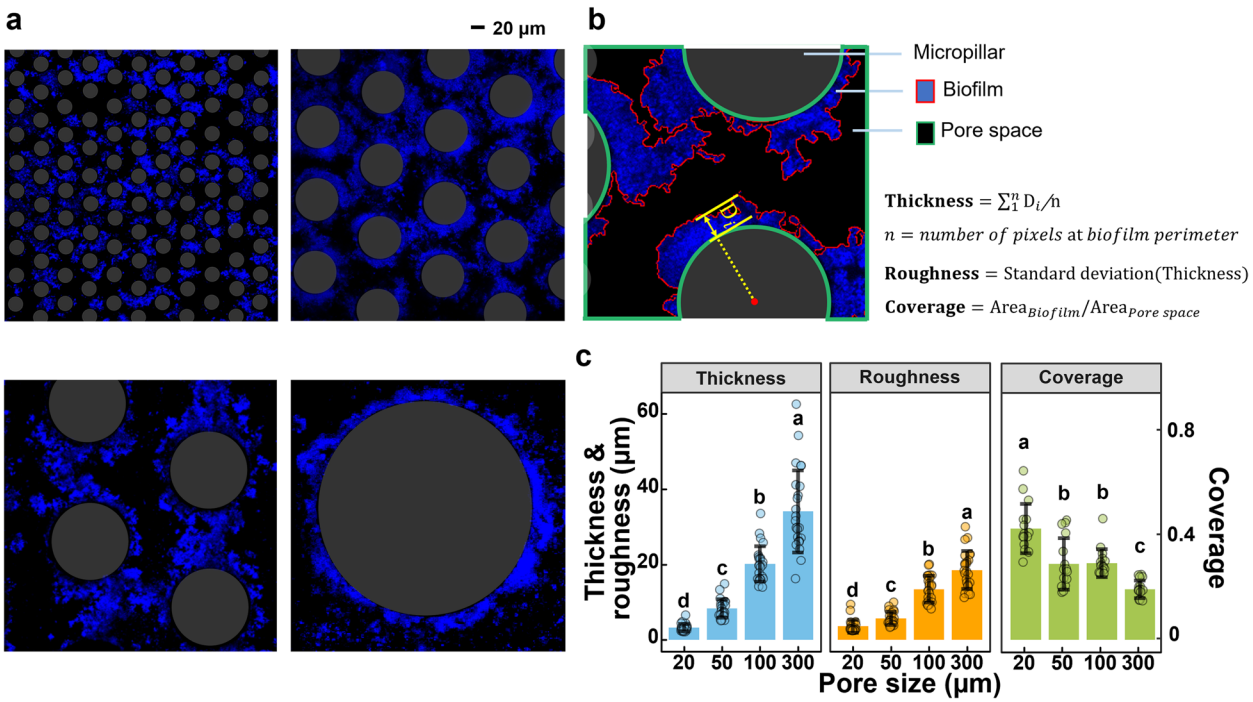

Fig. 2 Biofilm development in the microfluidic chip. Biofilm morphologies in different pore spaces (**a**). Biofilm cells were stained with DAPI. Schematic diagram illustrating biofilm morphology and coverage analysis (**b**). Biofilm thickness was calculated as the average radial distance from the biofilm perimeter to the micropillar surface, while roughness was quantified as the standard deviation of biofilm thickness on individual micropillar surfaces. Coverage represents the proportion of pore space occupied by biofilm. The biofilm thickness, roughness, and coverage in different pore environments (**c**). Data are presented as mean ± standard deviation. Biofilm morphology and coverage were assessed using images sampled from random areas within three independent biological replicates per pore space. Twenty-five observations per group were analyzed for biofilm thickness and roughness, while 15 observations per group were collected for biofilm coverage analysis. Different letters indicate significant differences ($p < 0.05$, one-way ANOVA)

a higher biofilm coverage compared to that at the pore size of 300 μm (Fig. 2a). Biofilms in distinct pore spaces also displayed varying compositions of extracellular polymeric substances (EPS), with larger pore sizes exhibiting a higher proportion of polysaccharides and proteins and a decreased proportion of extracellular DNA (eDNA) (Supplementary Figs. S4, S5, & S6). This suggests that the larger pore space not only enhances biofilm formation by increasing its thickness and roughness but also alleviates spatial constraints, leading to a reduced biofilm coverage within the pore spaces.

Reduced community evenness and increased phylogenetic diversity within larger pore spaces

The biofilm communities in different porous media were profiled using 16S amplicon sequencing. The Shannon diversity index, which considers both the number of distinct amplicon sequence variants (ASVs) in the community (richness) and their relative abundances (evenness), was assessed to evaluate community diversity. The results showed that biofilms grown in porous environments exhibited significantly higher Shannon diversity and richness compared to those developed in flat flow chambers without micropillars (Supplementary Fig. S7). This suggests that the porous structure is critical in providing sufficient spatial niches to support diverse microbial communities. The Shannon diversity of biofilms in porous environments initially decreased as pore size increased from 20 to 100 μm but subsequently increased as pore size further expanded to 300 μm (Fig. 3a). This inverted trend was attributed to the reduced evenness and increased richness in larger pore spaces, which are positively and negatively correlated with the biofilm coverage, respectively (Fig. 3b & c). The community phylogenetic structure was assessed by calculating the abundance-weighted standardized effect size measures of the mean nearest taxon distance (weighted SES.MNTD), providing estimates for the phylogenetic relatedness within closely-related relatives. The weighted SES.MNTD values exhibited a negative correlation with biofilm coverage (Fig. 3d). Since high biofilm coverage corresponds to high spatial constraints in small pore spaces, it indicates that biofilm inhabitants under increased spatial

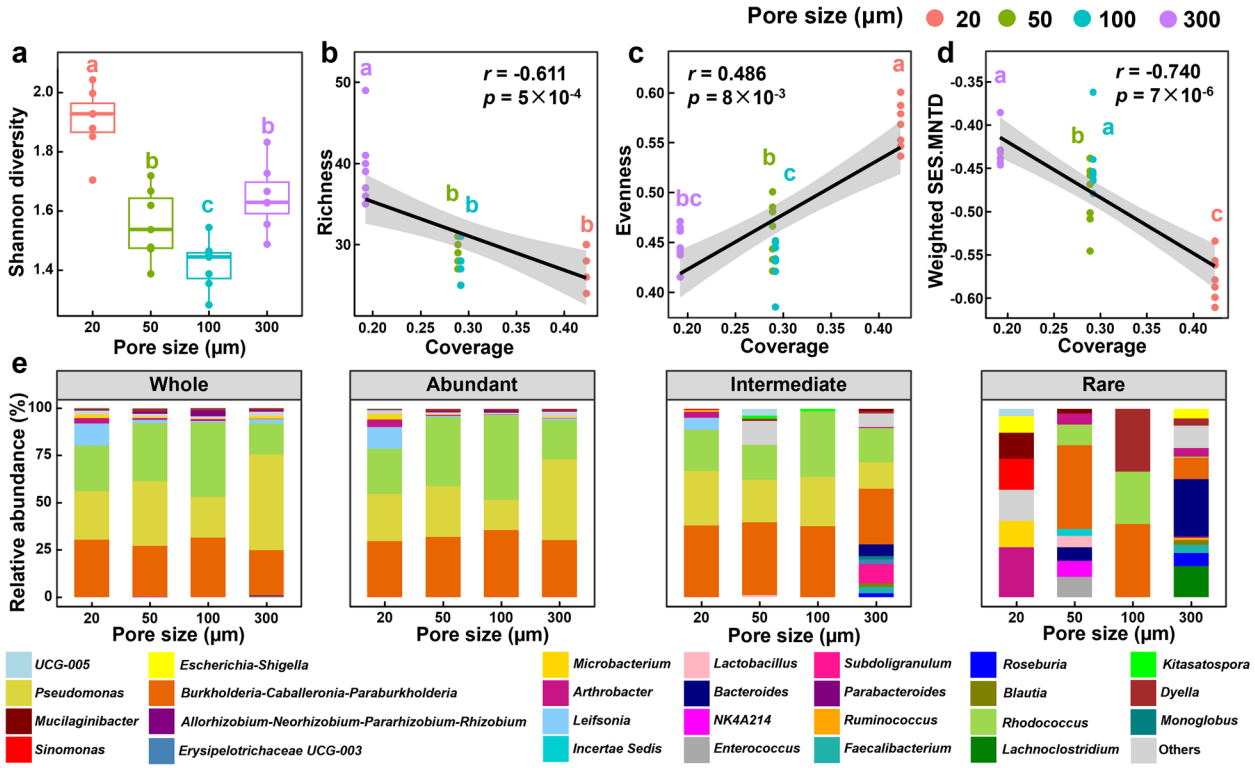

Fig. 3 Taxonomic and phylogenetic diversities of biofilms across different pore spaces. Shannon diversity of biofilm communities at varying pore sizes (**a**). Negative and positive correlations between community richness (**b**) and evenness (**c**) with biofilm coverage. Decreased abundance-weighted mean nearest taxon distance (weighted SES.MNTD) associated with higher biofilm coverage (**d**). *r* represents the Spearman correlation coefficient, and the shaded area indicates the 95% confidence interval. Different letters indicate significant differences ($p < 0.05$, one-way ANOVA, $n = 7$ independent biological replicates per pore size). Relative abundance of whole biofilm communities and subcommunities (abundant, intermediate, and rare) at the genus level (**e**)

constraints are phylogenetically closer and exhibit a more uniform distribution.

The analysis of community composition revealed that *Pseudomonas*, *Rhodococcus*, and *Burkholderia-Caballeronia-Paraburkholderia* were the most abundant genera across different pore spaces, constituting more than 80% of the whole biofilm communities (Fig. 3e). To further elucidate the difference in biofilms at different pore sizes, we compared the abundant (> 0.1%), rare (< 0.01%), and intermediate (0.1–0.01%) subcommunities classified based on the relative abundance of ASVs in respective porous environments. The Bray–Curtis similarity was calculated to quantify microbial composition similarities among these subcommunities across varying pore sizes. A total of 42.9% of abundant taxa were present across all pore spaces, contributing to a Bray–Curtis similarity of 0.7 ± 0.1 (Supplementary Figs. S8 & S9). Meanwhile, 85.4% of rare taxa were specific to their respective pore space, resulting in a markedly lower community similarity (Supplementary Figs. S8 & S9). The increased richness at the pore size of 300 μm was attributed to the significantly higher richness of all subcommunities compared to those in other pore spaces (Supplementary Fig. S10). In comparison to other pore spaces, the abundant subcommunities in 300-μm pore space contained more *Pseudomonas* and less *Rhodococcus*, while the intermediate subcommunities demonstrated higher proportions of *Bacteroides*, *Subdoligranulum*, and *Faecalibacterium* (Fig. 3e).

Stochastic processes drove biofilm community assembly

We employed the Sloan's neutral community assembly model to further elucidate the biofilm community assembly mechanism in different pore spaces. Microbial taxa occurring more or less frequently than expected were designated as above or below prediction, respectively. Based on the Akaike information criterion, the neutral community model outperformed the binomial distribution models, signifying the dispersal and ecological drift have a more significant impact than mere random sampling of the source metacommunity (Supplementary Fig. S11). The biofilm communities at the pore size of 20 μm exhibited the highest coefficient of the neutral fit. Increasing pore size led to a decline in the neutral model's explanatory power over community variance (79.9% to 31.6%) and the predicted proportion of microbial taxa (79.5 to 61.4%) (Fig. 4a, b, c, d), implying a reduced role of stochastic processes in biofilm assembly within larger pore spaces. At the pore size of 300 μm, the number of intermediate taxa that occurred more frequently than the prediction was increased, whereas more abundant ASVs, predominantly assigned to the genera *Burkholderia-Caballeronia-Paraburkholderia* and *Pseudomonas*, were less frequent than expected compared to other pore spaces (Fig. 4e, f, g, h, i, j, k, l). It suggests that these intermediate taxa possess higher migration ability to disperse more widely within the large pore space, while more abundant taxa exhibit lower dispersal ability and are selected against in the large pore space compared to non-abundant taxa. This trend is also corroborated by habitat specialization analysis, which reveals a decreased relative abundance of generalists (those adaptable to diverse habitats) and a concurrent increase in the proportion of opportunists (those falling between generalists and specialists) within the larger pore spaces (Supplementary Fig. S12).

We further investigated the co-occurrence patterns to elucidate the potential ecological interactions among biofilm communities in distinct pore spaces. The network of taxa at the pore size of 300 μm demonstrated the greatest complexity and connectivity because of the highest number of nodes and edges (Fig. 5, Supplementary Table S1). The network topological features, including average path length and network diameter, demonstrated reduced values for communities within the larger pore sizes (100 μm and 300 μm) compared to those within the smaller pore sizes (20 μm and 50 μm) (Supplementary Table S1). Additionally, the rare taxa in the pore size of 300 μm exhibited more associations between abundant and intermediate subcommunities (Fig. 5h), indicating a higher level of interconnectedness among these subcommunities. Conversely, the network for biofilm communities in the pore size of 20 μm exhibited the least nodes and edges, along with the lowest clustering coefficient, which quantifies the likelihood of two nodes sharing a common neighbor being connected (Supplementary Table S1). This suggests that the larger pore space with reduced spatial constraints facilitates a wide range of interactions, while the biofilm inhabitants within the confined pore space exhibit a low degree of association.

Increased pore space enhanced function redundancy and exometabolite diversity

To reveal the functional traits of biofilms assembled in different pore spaces, microbial functional potentials were predicted based on the 16S amplicon sequencing using Tax4Fun2. At the level 2 of KEGG category, genes associated with basic nutritional metabolism and genetic information processing, including carbohydrate, nucleotide and glycan metabolism, membrane transport, translation, and replication, were found to be more abundant in the biofilm at the 20-μm pore size compared to those in the larger pore space (Supplementary Fig. S13). Meanwhile, the biofilm in 300 μm exhibited the highest relative abundance in pathways related to environmental information processing and cellular processes, including

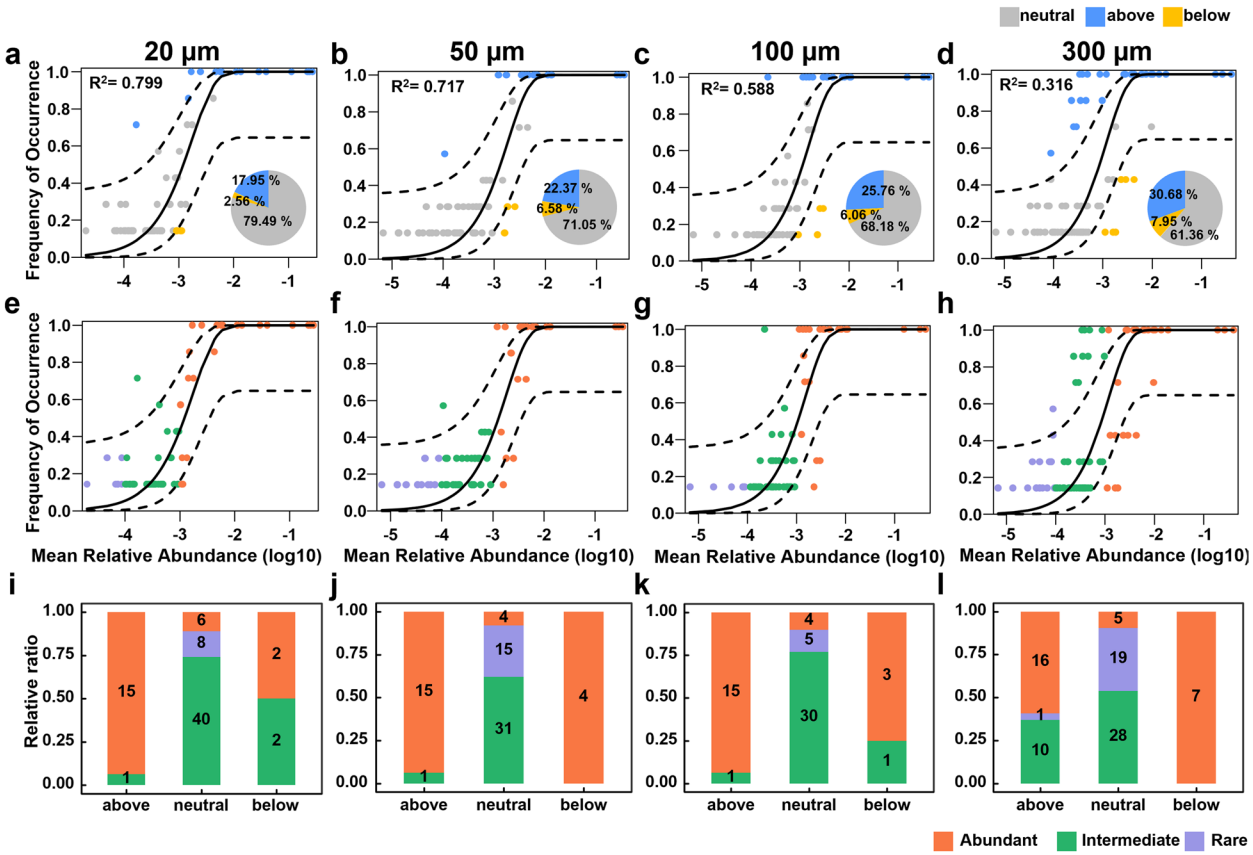

Fig. 4 Fit of the Sloan neutral community model. Each point represents a bacterial ASV at the pore size of 20 μm (**a**, **e**), 50 μm (**b**, **f**), 100 μm (**c**, **g**), and 300 μm (**d**, **h**). Dashed lines illustrate 95% confidence intervals around the model prediction. ASVs that occur more frequently and less frequently than the prediction are shown in blue and yellow, respectively (**a**, **b**, **c**, **d**). The R^2 demonstrates the goodness of fit to the neutral model. The inset pie chart reveals the proportion of ASVs below, within, and above neutral expectations. The abundant, intermediate, and rare ASVs were colored as orange, green, and purple, respectively (**e**, **f**, **g**, **h**). Relative abundance of different subcommunities that fall below, within, and above neutral model expectation (**i**, **j**, **k**, **l**). The numbers in the column denote the count of ASVs

biofilm development, signal transduction, and cell motility (Supplementary Fig. S13). The analysis of functional redundancy (FR), based on the average phylogenetic distance of community members possessing the same function, revealed a larger proportion of functions exhibiting higher FR within the biofilm at the 300-μm pore size than those in smaller pore spaces (Supplementary Fig. S14). Consequently, the phylogenetically diverse biofilm community at the pore space of 300 μm exhibits higher multifunctional redundancy.

As the functional predictions derived from amplicon sequencing do not accurately reflect the functions actively expressed, we profiled the exometabolites within the effluent from the microfluidic chips via metabolomics to elucidate the metabolic functionalities. Procrustes analysis revealed a strong correlation between these distinct exometabolic profiles and biofilm community structure (Fig. 6a). The Shannon diversity of the metabolome at the 300-μm pore space was significantly higher than those in smaller pore spaces, aligning with the increased biofilm community richness (Figs. 3b & 6b). Enrichment analysis was performed to identify metabolic pathways significantly enriched within different pore spaces with respect to fresh ISEM (Fig. 6c). Biofilms within 20-μm pore space exhibited the least number of enriched pathways, with a lower enrichment ratio compared to those observed in larger pore spaces. Notably, biofilms residing in 300-μm pore space displayed unique and significant enrichment in pathways associated with D-arginine and D-ornithine, butanoate, and alanine, aspartate, and glutamate metabolism, suggesting distinct metabolic features for biofilms residing in the largest pore spaces (Fig. 6c).

Discussion

Porous environments serve as the predominant habitats for microbes [1, 18]. The intricate pore structures within these environments modulate diverse microbial interactions and foster the development of complex microbial

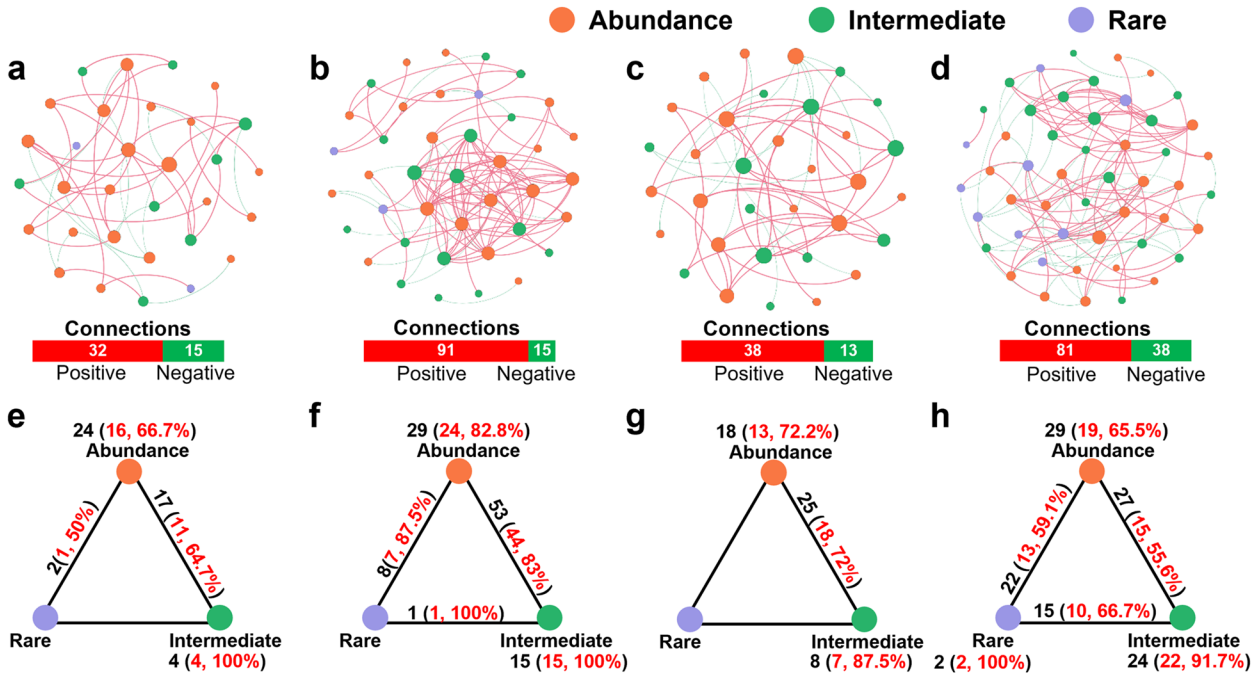

Fig. 5 Network associations of bacterial ASVs in different pore spaces. Co-occurrence networks were constructed using Spearman's rank correlation to identify strong and significant correlations (Spearman's $r > 0.5$ and $p < 0.05$) (**a**, **b**, **c**, **d**). The node color represents the abundance categories of the ASV, and the node size is proportional to its degree. The connection thickness reflects the strength of Spearman's correlation coefficients. A red connection indicates a positive correlation, while a green connection denotes a negative correlation. The bar graph presents the total number of positive and negative connections within each porous environment. Summaries of node-connection statistics (**e**, **f**, **g**, **h**). The black numbers indicate the total number of connections within and between subcommunities, and the red numbers in parentheses represent the count and percentage of positive connections

communities [19]. However, the role of pore space in shaping biofilm community structure and function remains largely unexplored. In this study, we employed laboratory-constructed microfluidic chips to investigate the assembly mechanisms of soil microbial biofilm communities in pore spaces under different levels of spatial constraints. The biofilm in smaller pore spaces exhibited reduced thickness and roughness while also demonstrating greater coverage by forming a streamer structure within these spatially confined pore spaces. Increasing the pore size led to a decrease in biofilm community evenness and a concomitant increase in phylogenetic diversity. The biofilm inhabiting the 300-μm pore space exhibited significantly higher richness compared to those in smaller pore spaces. The neutral model analysis revealed a diminishing contribution of stochastic processes in biofilm community assembly with increasing pore space. Exometabolomic analyses further revealed a significant correlation between exometabolite pools and biofilm community structure. A significantly higher exometabolome diversity was observed in the 300-μm pore space which associated with the increased biofilm community richness. Together, these results reveal that large pore spaces with reduced spatial constraints promote biofilm formation and foster the assembly of a more diverse microbial community, both in terms of phylogenetic composition and functional attributes.

Soil biofilms typically range from 10 to 100 μm in thickness [1, 20]. In this study, we fabricated microfluidic chips with pore sizes ranging from 20 to 300 μm to impose varying degrees of spatial constraints on soil biofilm development. According to soil pore size classification, pores between 10 and 50 μm were designated as small coarse pores, while those higher than 50 μm were defined as wide coarse pores [21]. These pore size ranges correspond to mechanical fissures, cracks, and biopores (from roots and earthworms), which are known hotspots for soil biofilm formation. Previous studies have reported divergent effects of pore space on microbial diversity [5, 22–24]. These varying results were generally attributed to complex organic pools, different microbial communities, and distinct mineral compositions. To isolate the effect of pore space geometry, we investigated the biofilm assembly across different pore spaces with identical pore water chemistry, solid substratum, and inoculum community composition. Our findings revealed that the smaller pore size led to reduced community richness and phylogenetic diversity. Consistent with our findings, a previous

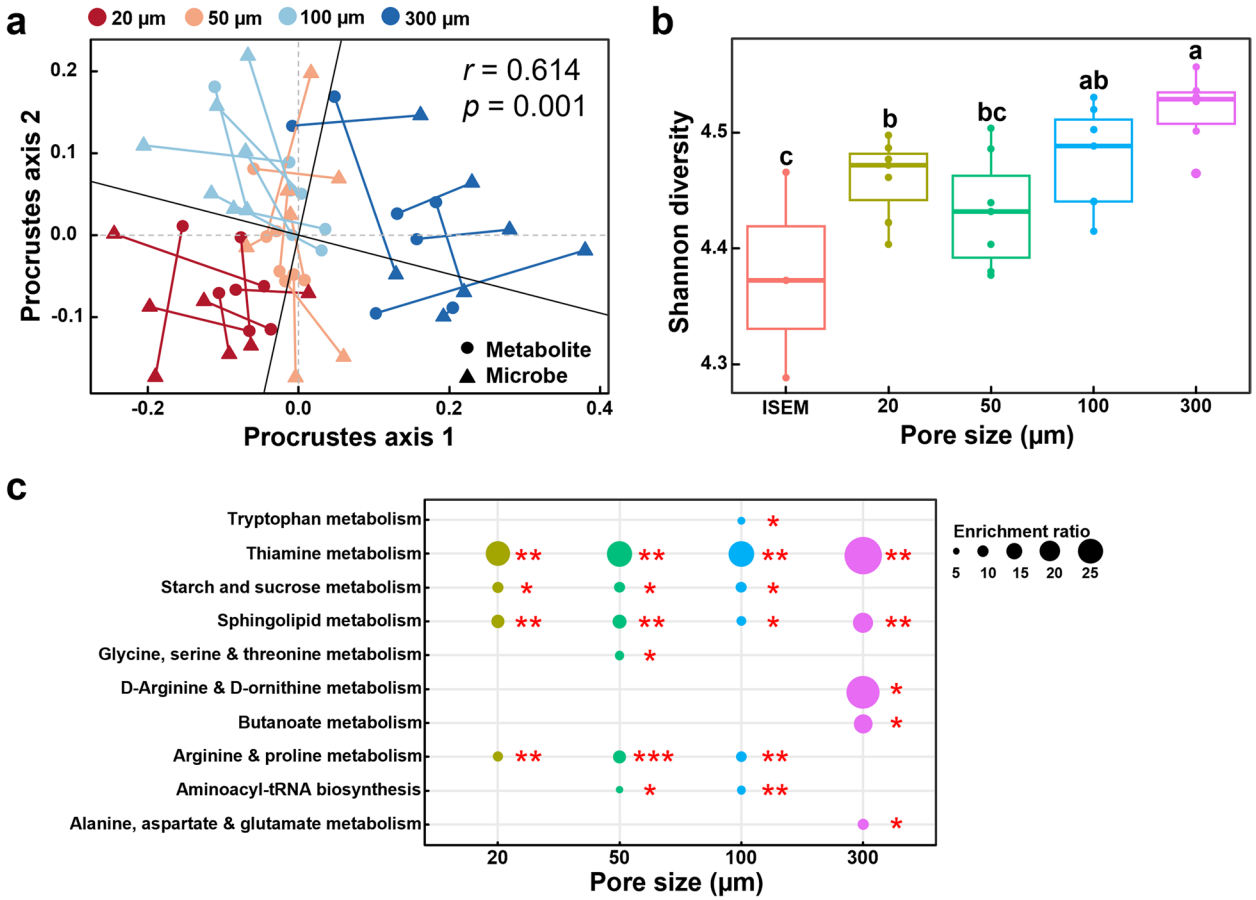

Fig. 6 Enhanced exometabolite diversity in large pore spaces. Procrustes analysis revealing the significant correlation between microbial communities and exometabolite profiles (**a**). The Shannon diversity of the exometabolites in different pore spaces (**b**). Enrichment analysis of exometabolomic data with respect to fresh ISEM (**c**). The bubble size corresponds to the pathway enrichment ratio for differentially abundant metabolites across various pore spaces. Asterisks denote statistically significant differences based on the hypergeometric test (***$p \le 0.001$, **$p \le 0.01$, *$p \le 0.05$, $n = 7$ independent biological replicates per pore size)

study in bermudagrass ecosystems identified soil texture as the second most influential factor (after pH) shaping soil microbial communities, with clay content exhibiting negative and positive correlations with bacterial richness and evenness, respectively, particularly under wet conditions [24]. Our analyses further revealed that a stronger fit (R^2) for the Sloan's neutral community model within the smaller pore spaces indicates the colonization is predominantly governed by a stochastic, birth–death immigration process (Fig. 4a, b, c, d) [25]. Deterministic processes, such as microbial interactions, appear to exert less influence on biofilm assembly in confined porous environments. The diminished importance of microbial interaction in shaping biofilm community can be attributed to biofilm clogging, which hindered nutrient diffusion and metabolite exchange among biofilm inhabitants. Consequently, the enhanced microbial diversity within confined pore spaces observed in previous studies may arise from factors beyond pore size.

Meanwhile, a significant increase in community richness was observed at the 300-μm pore size. Neutral model analysis revealed a higher number of abundant taxa were selected against, while more intermediate taxa were actively selected at the pore size of 300 μm comparing to smaller pore spaces (Fig. 4i, j, k, l). It indicates that abundant taxa were incapable of occupying all niches within the large pore space, thereby enabling the growth of intermediate taxa. This observation aligns with the reduced proportion of generalists and the increased proportion of opportunists as pore size expands (Supplementary Fig. S12). Metabolomic analysis of the 300-μm pore space unveiled greater chemical diversity within the exometabolome and the emergence of unique metabolic pathways not observed in other small pore spaces, indicating extensive metabolic interactions in the large pore space. These interactions were further supported by the highest level of network complexity and connectivity

observed in co-occurrence analysis (Fig. 5, Supplementary Table S1). It suggests that large pore spaces can provide more spatial niches to facilitate the colonization of non-abundant taxa and foster the coexistence of phylogenetically distant taxa.

These findings have significant implications for the management, control, and engineering of biofilms in porous environments. In confined pore spaces, increased biofilm coverage reduces pore connectivity, inhibiting biofilm activity and leading to simpler, more homogeneous communities. Consequently, biofilms in such environments are more susceptible to removal by biocidal agents. In contrast, biofilms in larger pore spaces exhibit elevated EPS content, making EPS targeting crucial for effective biofilm eradication. Furthermore, sufficient pore space supports the development of thicker and more metabolically diverse biofilms, suggesting that increasing pore space may be an effective strategy for enhancing biofilm functionalities. Previous studies have highlighted the superior performance of large-pore membrane bioreactors and macroporous biofilm carriers in contaminant removal through biocatalysis [26, 27].

This study has elucidated the influence of pore sizes on biofilm community assembly and function traits using a combined microfluidic and multi-omics approach. Future metagenomic studies could further characterize the genomic functional potential of biofilms formed in varying pore sizes and at different growth stages. These genomic data could corroborate the observed relationship between pore size and genomic functional potential, particularly the increased functional redundancy within larger pores that may enhance community resilience to environmental perturbations, such as fluctuations in pore water and nutrient availability, antimicrobial agent exposure, and microbial invasion. Further investigation is warranted into the spatial organization of different biofilm inhabitants within pore spaces and their mutual interactions. The spatial structure of complex biofilm communities can be visualized using techniques such as fluorescent gene tagging and high-phylogenetic-resolution microbiome mapping by fluorescence in situ hybridization (HiPR-FISH) [28]. Additionally, the effects of other key physicochemical factors on biofilm development within porous ecosystems can be investigated by leveraging microfluidic platforms. For example, substratum properties can be assessed by coating the internal surfaces of microfluidic devices with polymers or minerals through direct adsorption or light curing. Flow conditions can be precisely controlled to study hydrodynamic influences, including the impact of varying shear forces or unsaturated microenvironments.

Conclusions

Our study demonstrates that the physical structure of porous environments plays a critical role in shaping biofilm community structure, assembly processes, and functional diversity. By employing microfluidic chips with controlled pore sizes, we observed that larger pore spaces increased biofilm thickness and roughness, while decreasing biofilm coverage and alleviating spatial constraints. Larger pore size resulted in reduced biofilm community evenness and increased phylogenetic diversity, with deterministic processes exerting a greater influence on community assembly. Exometabolomic analyses of effluents from the microfluidic chips further elucidated a significant correlation between the exometabolite profiles and biofilm community structure. The increased community richness in large pore spaces was associated with the significantly higher exometabolome diversity. These findings highlight that mitigating spatial constraints in porous environments promotes the development of biofilms with greater phylogenetic and functional diversity, providing insights into managing microbial communities across environmental, industrial, and medical contexts.

Methods

Soil sampling

Soil samples were collected from the woodland topsoil (0–20 cm) at Qiyang Red Soil Experimental Station (Hunan province, China, 111°53′E, 23°27′N) in Mar 2021. The samples were cleaned of stones and roots and then homogenized by sieving through a 2-mm mesh.

Soil bacteria extraction and growth medium preparation

Soil microorganisms were extracted from the collected soil samples using Nycodenz gradient centrifugation [29]. Intensive soil extract medium (ISEM) was prepared as described in a previous study to cultivate soil microbial communities [30, 31]. Briefly, 500 g of dry soil was subjected to two rounds of extraction with 1.3 L of 80% methanol to yield the supernatant, which was subsequently filtered and lyophilized. The lyophilized soil extract was redissolved in 200-mL water and filtered through a 0.22-μm filter to obtain the soil extract solution. ISEM contained 20% soil extract solution, 0.1% mineral salt solution, 0.1% vitamin stock solution, 0.2% selenite-tungstate solution, and 0.2% trace element solution SL-10. The pH of the ISEM was adjusted to 6.8. The ingredient details are available in the supplementary information (Supplementary Table S2).

Microfluidic chip fabrication

Microfluidic chips with arrays of micropillars were fabricated to simulate the porous architecture of soil. Four different microfluidic chips were designed with

micropillars of 20, 50, 100, and 300 μm in diameter and height, respectively (Supplementary Fig. S1). The corresponding volumes of these microfluidic chambers were 1.2 μL, 3.0 μL, 6.0 μL, and 18.0 μL. To investigate the influence of the porous environment on biofilm development, control flow chambers with identical dimensions but without micropillars were also fabricated (Supplementary Fig. S15). The direct-write photolithography (MicroWriter ML3) and deep reactive ion etching (DRIE) were employed to create the microchannel features on silicon wafers. PDMS prepolymer was poured over the silicon wafers, degassed under vacuum, and cured in an oven at 80 °C for at least 2 h. The structured PDMS was then peeled off and bonded to a glass slide after plasma treatment to construct the microfluidic devices. The microfluidic chips were sterilized with 75% ethanol prior to inoculation.

Biofilm development in microfluidic chips

The microfluidic chip consisted of a flow channel with two inlets and one outlet (Supplementary Fig. S1). One of the inlets was connected to a syringe pump to supply fresh ISEM for microbial growth, while the other inlet was used for inoculation. The collected soil microbial cells were precultivated in ISEM and then resuspended in phosphate-buffered saline (PBS) to an OD600 of 0.1. Subsequently, 50, 125, 250, and 750 μL of soil bacterial suspension were introduced into microfluidic chips with micropillars of 20, 50, 100, and 300 μm in diameter, respectively. The inoculation port was sealed with PDMS after inoculation. Microbial cells were allowed to stand for 2 h to facilitate initial attachment to the substratum [30]. Afterward, sterile ISEM was introduced into the microfluidic chambers for biofilm cultivation at 25 °C in the dark. To maintain a constant retention time across different microfluidic chambers, ISEM was then supplied to microfluidic chips with micropillars of 20, 50, 100, and 300 μm at flow rates of 0.2, 0.5, 1, and 3 μL/min, respectively. Before sampling, the tubing and needles at the outlet were replaced with sterile ones, and two sterile syringes were connected to the inlet and outlet of microfluidic chamber. One milliliter of PBS buffer was repeatedly flushed between these two syringes to extract microbial cells in the microfluidic chamber. Seven independent biological replicates were conducted for each microfluidic design.

Confocal microscopy and image processing

Biofilms in microfluidic chips were visualized using a confocal microscope (AIR, Nikon) after fluorescent staining. The biofilm cells, protein, polysaccharide, and eDNA were stained with DAPI, SYPRO Orange, Concanavalin A (Con A), and 7-hydroxy-9H-(1,3-dichloro-9,9-dimethylacridin-2-one) (DDAO), respectively. Biofilm thickness and roughness were calculated as previously described [30]. The proportional composition of each EPS component was determined by dividing its fluorescent area by the total fluorescent area of the biofilm cells. Biofilm coverage was calculated as the ratio of the biofilm area to the pore area.

16S rRNA amplicon sequencing

We performed 16S rRNA amplicon sequencing to evaluate the biofilm communities assembled in different porous environments. Total DNA was extracted with the EZNA Soil DNA Kit (Omega). The V3–V4 regions of bacterial 16S rRNA gene were amplified using the primer pair 338F (5′-ACTCCTACGGGAGGCAGC A-3′) and 806R (5′-GGACTA CHVGGGT WTCTAT -3′) [32]. The thermal conditions for amplification were as follows: initial denaturation at 98 °C for 2 min; 25 cycles at 98 °C for 15 s, 55 °C for 30 s, and 72 °C for 30 s; and final elongation at 72 °C for 30 s. The PCR amplicons were purified with VAHTS™ DNA Clean Beads (Vazyme) and then sequenced on the Illumina MiSeq PE300 platform.

Exometabolomic analysis

Prior to extracting microbial communities from microfluidic devices, 100 μL of effluent was collected at the outlet for metabolomic analysis. The effluent was passed through a 0.2-μm filter to remove bacterial cells. The filtrate was then vortexed with 400 μL of pre-cooled methanol/acetonitrile/water solution (2:2:1, v/v/v), incubated at − 20 °C for 10 min, and centrifuged at 14,000 g at 4 °C for 20 min. The supernatant was dried in vacuum and redissolved in 100 μL of acetonitrile aqueous solution (acetonitrile:water = 1:1, v/v). After centrifuged at 14,000 g at 4 °C for 15 min, the supernatant was subjected to LC–MS/MS analysis. Quality control (QC) samples were prepared by combining equal aliquots from all effluent samples and measured before analysis and after every 10 runs to evaluate the analytical variance. The metabolomic features were characterized using ultrahigh performance liquid chromatography-tandem time-of-flight mass spectrometry (UHPLC-Q-TOF MS). The ESI source temperature was set to 600 °C, with the ion spray voltage floating at 5500 V in both positive and negative modes. TOF MS scan m/z range was 60–1000 Da, and the product ion scan m/z range was 25–1000 Da.

Metabolomic data analysis

ProteoWizard was used to convert the raw data into mzXML format, which was then processed by XCMS for peak alignment. XCMS was configured with the following settings: method = "centWave", ppm = 10, peakwidth = c

(10, 60), prefilter = c (10, 100), mzwid = 0.025, minfrac = 0.5, and bw = 5. Only metabolites at level 2 identification (putatively annotated compounds) were used for downstream analysis. The differentially abundant metabolites (DAMs) in the effluents, relative to ISEM, were identified through OPLS-DA and *t*-test ($VIP > 1$, $p < 0.05$). Metabolic pathway enrichment analysis was carried out using the MetaboAnalyst 5.0 web-based platform (www.metaboanalyst.ca) to determine the KEGG metabolic pathways significantly enriched in the DAMs [33].

Bioinformatic analysis

The raw amplicon sequencing data were processed using the DADA2 plugin in QIIME2 (https://view.qiime2.org) [34, 35]. The Cutadapt plugin was employed to trim the primers (cutadapt trim-paired) [36]. The sequences were then denoised using DADA2 based on the quality score, clustered into amplicon sequence variants (ASVs), and rarefied to the minimum number of reads per sample (21,247 reads). The ASV sequences were aligned to a pre-trained SILVA database using the QIIME2 feature-classifier plugin (release 138, bacteria) [37]. Richness and Shannon diversity indices were calculated using the vegan package [38]. Following the classification in the previous studies [39], ASVs were categorized as abundant (> 0.1%), rare (< 0.01%), or intermediate (0.01–0.1%) based on their relative abundances in each porous media. The functional profiles of microbial communities were predicted by Tax4Fun2 [40]. Co-occurrence networks were constructed using Spearman's rank correlation coefficients between ASVs present in at least two samples. Only robust correlations ($|r| > 0.5$) with statistically significant ($p < 0.05$) were included in the networks. The networks were visualized using the interactive platform Gephi [41–43]. Network topological features, including the number of nodes and edges, modularity, average clustering coefficient, network diameter, average path length, and average degree, were analyzed using Gephi. Phylogenetic diversity was evaluated through the abundance-weighted standardized effect size measures of the mean nearest taxon distance (weighted SES.MNTD), using the picante package [44].

Community assembly analysis

The Sloan neutral community model (NCM) was employed to elucidate the assembly mechanisms of communities in different porous environments [25, 45]. The relationship between ASV occurrence frequency and their relative abundance across the wider metacommunity was predicted to determine the contribution of stochastic process. The goodness of fit to the neutral model was assessed using R^2 through nonlinear least-squares fitting. Bacterial taxa exceeding, aligning with, or falling below the model-predicted expectations were identified by comparing their frequencies with the 95% confidence interval limits of this best-fit neutral model. The fit of the neutral model was compared with that of the binomial distribution model to determine the effects of ecological drift and dispersal limitation on community assembly [46].

Habitat specialization analysis

The assessment of habitat specialization was conducted using Levins' niche breadth [47]. Levins' niche breadth was calculated as follows:

$$B_j = \frac{1}{\sum_{i=1}^{N} P_{ij}^2}$$

where B_j indicates the niche breadth of ASV j, N is the total number of communities, and P_{ij} is the proportion of ASV j in community i. Niche breadth was calculated based on the relative abundance of ASVs within each porous environment. The occurrences of ASVs wer generated by the simulation of 1000 permutations using the quasiswap algorithm of the EcolUtils R package [48]. ASVs are defined as generalists if their observed occurrence surpasses the upper limit of the 95% confidence interval. Conversely, any ASV with observed occurrence below the lower 95% confidence interval is categorized as a specialist. ASVs with occurrences within the 95% confidence interval are considered opportunist taxa [49].

Sample size determination

Previous research has suggested using more than five biological replicates in amplicon sequencing to detect differences in microbial communities effectively [50]. In this study, we used seven biological replicates in our amplicon sequencing experiments to enhance data comparability and achieve higher resolution in differentiating the effects of varying pore sizes. To evaluate the significance of pore space effects on community structure across different biological replicates, we conducted three nonparametric analyses: nonparametric multivariate ANOVA using distance matrices (Adonis), analysis of similarity (ANOSIM), and multiresponse permutation procedure (MRPP). The Bray–Curtis similarity index was used to construct the distance matrix for all three analyses. Statistical significance was assessed using Monte Carlo permutations. All analyses were conducted using the vegan package [38]. By comparing community structures across different numbers of biological replicates, we confirmed that seven replicates were sufficient to distinguish differences in community structures

(Supplementary Table S3). Furthermore, we conducted a power analysis to determine the appropriate sample size for imaging analysis. Using a significance level of 0.05, a statistical power of 0.8, and an effect size of 0.5 across four groups, the power analysis indicated that 12 observations per group were necessary. Based on these results, we collected 15 observations per group for EPS and biofilm coverage analysis and 25 observations per group for biofilm thickness and roughness analysis from random areas within three biological replicates.

Supplementary Information

The online version contains supplementary material available at https://doi.org/10.1186/s40168-025-02075-0.

Supplementary Material 1: Supplementary Fig. S1. Microfluidic chips with micropillar arrays designed to simulate porous environments. The chip features micropillars with diameters of 20, 50, 100, and 300 µm, with corresponding heights. It includes one outlet, one inoculation port, and one medium inlet. The inoculation port is positioned downstream of the medium inlet to prevent contamination. The pore size is defined by the minimum spacing between adjacent micropillars (a). Top views (b-e) and side views (f-i) of microfluidic chips with micropillars of varying diameters. Microscopic top-down views (j-m) and scanning electron microscopy (SEM) images (n-q) of the micropillar arrays. Supplementary Fig. S2. Flowchart illustrating the experimental design. A soil microbial community was extracted and cultured in microfluidic chips with varying pore sizes using a soil extract medium derived from the same soil sample. Following biofilm development, biofilm morphologies were imaged, microbial community compositions were analyzed via 16S amplicon sequencing, and functional properties were assessed using exometabolomics. Supplementary Fig. S3. The development of biofilm architecture in the porous environment of various sizes: 20 µm (a), 50 µm (b), 100 µm (c), and 300 µm (d), respectively. Supplementary Fig. S4. 3D visualization of biofilms grown in microfluidic chips with varying pore sizes. Biofilms were stained with DAPI (blue) for cells, SYPRO Orange (green) for proteins, Concanavalin A (Con A, red) for polysaccharides, and 7-hydroxy-9H-(1,3-dichloro-9,9-dimethylacridin-2-one) (DDAO, purple) for eDNA. Supplementary Fig. S5. Orthogonal views of biofilms grown in the microfluidic chips with different pore sizes. Supplementary Fig. S6. The relative abundance of different EPS components in biofilms. Extracellular proteins, polysaccharides and eDNA were stained with fluorescent dyes. The relative abundance of each EPS component was determined as the ratio of its fluorescence area to the total fluorescence area of biofilm cells. 15 observations per group were collected for EPS analysis. Different letters indicate significant differences ($p < 0.05$, one-way ANOVA). Supplementary Fig. S7. Biofilms developed in microfluidic chips with porous structures exhibit significantly higher Shannon diversity (a), richness (b), and evenness (c) compared to those in flat chambers. Different letters indicate significant differences ($p < 0.05$, one-way ANOVA). Supplementary Fig. S8 Pairwise comparison of Bray-Curtis similarity between different porous environments for abundant (a), intermediate (b) and rare taxa (c). Significance of results was evaluated using ANOVA and indicated by different letters. Supplementary Fig. S9 Venn diagram illustrating the numbers of unique and shared ASVs among various porous environments for different subcommunities: Abundant (abundant taxa), Intermediate (intermediate taxa), Rare (rare taxa), and Whole (all bacterial taxa). Supplementary Fig. S10 The taxonomic richness diversity across different porous environments for abundant, intermediate, and rare taxa. Statistical significance was assessed using ANOVA, with different letters indicating significant differences. Supplementary Fig. S11 Comparison of the maximum likelihood fit between the neutral and binomial models. Supplementary Fig. S12 Relative abundance of generalists, opportunists and specialists in respective porous environments. Significant differences were evaluated using ANOVA and denoted with different letters. Supplementary Fig. S13 Relative abundances of KEGG level2 pathways. Different letters indicate significant differences ($p < 0.05$, one-way ANOVA). Supplementary Fig. S14 Differences in functional redundancy in different pore environments. 300 µm vs 20 µm (a); 300 µm vs 50 µm (b); 300 µm vs 100 µm (c). A log ratio greater than zero denotes greater functional redundancy in the 300 µm pore environment. Supplementary Fig. S15 The photograph of control microfluidic chips without micropillar arrays. Top view of the microfluidic chips (a-d). Cross-sectional view of the flat chambers with varying heights (e-h). Supplementary Table S1. Network-level topological features. Supplementary Table S2. Recipes for soil extract solutions. Supplementary Table S3. Significance tests of pore space effects on the biofilm community structure across different biological replicate numbers and statistical approaches.

Acknowledgements
Confocal laser scanning microscopy (CLSM) images were acquired at the National Key Laboratory of Agricultural Microbiology Core Facility.

Authors' contributions
Y.W. and P.C. conceived and designed the project. Y.W. and C.F. performed the experiments and analyzed the data. Y.W., P.C., and C.F. wrote the paper with input from all authors.

Funding
This work was supported by the National Natural Science Foundation of China (42225706, 42177281, 42177283, 42377297), the National Key Research Program of China (2020YFC1806802), and Fundamental Research Funds for the Central Universities (2662022ZHYJ001, 2662021JC012).

Data availability
The raw amplicon sequencing data have been deposited in the NCBI SRA database with the BioProject accessions PRJNA1110568. The CLSM microscopic images and computer code used for image processing and the Sloan's neutral community assembly model analysis have been stored in the figshare database (https://figshare.com/projects/The_mitigation_of_spatial_constraint_in_porous_environments_enhances_biofilm_phylogenetic_and_functional_diversity/211720).

Declarations

Ethics approval and consent to participate
Not applicable.

Consent for publication
Not applicable.

Competing interests
The authors declare no competing interests.

Received: 17 July 2024 Accepted: 27 February 2025
Published online: 24 March 2025

References

1. Flemming HC, Wuertz S. Bacteria and archaea on earth and their abundance in biofilms. Nat Rev Microbiol. 2019;17:247–60.
2. Kolter R, Greenberg EP. The superficial life of microbes. Nature. 2006;441:300–2.
3. Flemming H-C, Baveye P, Neu TR, Stoodley P, Szewzyk U, Wingender J, et al. Who put the film in biofilm? The migration of a term from wastewater engineering to medicine and beyond. NPJ Biofilms Microbiomes. 2021;7:10.
4. Kurz DL, Secchi E, Carrillo FJ, Bourg IC, Stocker R, Jimenez-Martinez J. Competition between growth and shear stress drives intermittency in preferential flow paths in porous medium biofilms. Proc Natl Acad Sci USA. 2022;119:e2122202119.
5. Wilpiszeski RL, Aufrecht JA, Retterer ST, Sullivan MB, Graham DE, Pierce EM, et al. Soil aggregate microbial communities: towards understanding microbiome interactions at biologically relevant scales. Appl Environ Microbiol. 2019;85:e00324-e419.

6. Lee SH, Secchi E, Kang PK. Rapid formation of bioaggregates and morphology transition to biofilm streamers induced by pore-throat flows. Proc Natl Acad Sci USA. 2023;120:e2204466120.
7. Erktan A, Or D, Scheu S. The physical structure of soil: determinant and consequence of trophic interactions. Soil Biol Biochem. 2020;148:107876.
8. Long T, Or D. Aquatic habitats and diffusion constraints affecting microbial coexistence in unsaturated porous media. Water Resour Res. 2005;41:W08408.
9. Coyte KZ, Tabuteau H, Gaffney EA, Foster KR, Durham WM. Microbial competition in porous environments can select against rapid biofilm growth. Proc Natl Acad Sci USA. 2017;114:E161–70.
10. Wu F, Ha Y, Weiss A, Wang M, Letourneau J, Wang S, et al. Modulation of microbial community dynamics by spatial partitioning. Nat Chem Biol. 2022;18:394–402.
11. Bach EM, Williams RJ, Hargreaves SK, Yang F, Hofmockel KS. Greatest soil microbial diversity found in micro-habitats. Soil Biol Biochem. 2018;118:217–26.
12. Perujo N, Sánchez-Vila X, Proia L, Romaní AM. Interaction between physical heterogeneity and microbial processes in subsurface sediments: a laboratory-scale column experiment. Environ Sci Technol. 2017;51:6110–9.
13. Oliveira NM, Martinez-Garcia E, Xavier J, Durham WM, Kolter R, Kim W, et al. Biofilm formation as a response to ecological competition. PLoS Biol. 2015;13:e1002191.
14. Schluter J, Nadell CD, Bassler BL, Foster KR. Adhesion as a weapon in microbial competition. ISME J. 2015;9:139–49.
15. Burmølle M, Ren D, Bjarnsholt T, Sørensen SJ. Interactions in multispecies biofilms: do they actually matter? Trends Microbiol. 2014;22:84–91.
16. Scheidweiler D, Peter H, Pramateftaki P, de Anna P, Battin TJ. Unraveling the biophysical underpinnings to the success of multispecies biofilms in porous environments. ISME J. 2019;13:1700–10.
17. Li Z, Kravchenko AN, Cupples A, Guber AK, Kuzyakov Y, Philip Robertson G, et al. Composition and metabolism of microbial communities in soil pores. Nat Commun. 2024;15:3578.
18. Battin TJ, Besemer K, Bengtsson MM, Romani AM, Packmann AI. The ecology and biogeochemistry of stream biofilms. Nat Rev Microbiol. 2016;14:251–63.
19. Mason G, Footer MJ, Rojas ER. Mechanosensation induces persistent bacterial growth during bacteriophage predation. MBio. 2023;14:e02766-e2822.
20. Wu Y, Redmile-Gordon M, Cai P, Gao C, Huang Q. Soil biofilms: evolving concepts and ecological functions. Encyclopedia Soils Environ. 2023;1:120–6.
21. Totsche KU, Amelung W, Gerzabek MH, Guggenberger G, Klumpp E, Knief C, et al. Microaggregates in soils. J Plant Nutr Soil Sc. 2018;181:104–36.
22. Davinic M, Fultz LM, Acosta-Martinez V, Calderón FJ, Cox SB, Dowd SE, et al. Pyrosequencing and mid-infrared spectroscopy reveal distinct aggregate stratification of soil bacterial communities and organic matter composition. Soil Biol Biochem. 2012;46:63–72.
23. Seaton FM, George PB, Lebron I, Jones DL, Creer S, Robinson DA. Soil textural heterogeneity impacts bacterial but not fungal diversity. Soil Biol Biochem. 2020;144:107766.
24. Xia Q, Rufty T, Shi W. Soil microbial diversity and composition: links to soil texture and associated properties. Soil Biol Biochem. 2020;149:107953.
25. Sloan WT, Lunn M, Woodcock S, Head IM, Nee S, Curtis TP. Quantifying the roles of immigration and chance in shaping prokaryote community structure. Environ Microbiol. 2006;8:732–40.
26. Ji J, Sakuma S, Ni J, Chen Y, Hu Y, Ohtsu A, et al. Application of two anaerobic membrane bioreactors with different pore size membranes for municipal wastewater treatment. Sci Total Environ. 2020;745:140903.
27. Lu Z, Sun W, Li C, Cao W, Jing Z, Li S, et al. Effect of granular activated carbon pore-size distribution on biological activated carbon filter performance. Water Res. 2020;177:115768.
28. Shi H, Shi Q, Grodner B, Lenz JS, Zipfel WR, Brito IL, et al. Highly multiplexed spatial mapping of microbial communities. Nature. 2020;588:676–81.
29. Lindahl V, Bakken LR. Evaluation of methods for extraction of bacteria from soil. FEMS Microbiol Ecol. 1995;16:135–42.
30. Wu Y, Fu C, Peacock CL, Sørensen SJ, Redmile-Gordon MA, Xiao K-Q, et al. Cooperative microbial interactions drive spatial segregation in porous environments. Nat Commun. 2023;14:4226.
31. Nguyen TM, Seo C, Ji M, Paik M-J, Myung S-W, Kim J. Effective soil extraction method for cultivating previously uncultured soil bacteria. Appl Environ Microbiol. 2018;84:e01145-e1218.
32. Wu Y, Cai P, Jing X, Niu X, Ji D, Ashry NM, et al. Soil biofilm formation enhances microbial community diversity and metabolic activity. Environ Int. 2019;132:105116.
33. Pang Z, Chong J, Zhou G, de Lima Morais DA, Chang L, Barrette M, et al. MetaboAnalyst 5.0: narrowing the gap between raw spectra and functional insights. Nucleic Acids Res. 2021;49:W388–96.
34. Caporaso JG, Kuczynski J, Stombaugh J, Bittinger K, Bushman FD, Costello EK, et al. QIIME allows analysis of high-throughput community sequencing data. Nat Methods. 2010;7:335–6.
35. Callahan BJ, McMurdie PJ, Rosen MJ, Han AW, Johnson AJA, Holmes SP. Dada2: high-resolution sample inference from illumina amplicon data. Nat Methods. 2016;13:581–3.
36. Martin M. Cutadapt removes adapter sequences from high-throughput sequencing reads. EMBnet J. 2011;17:10–2.
37. Quast C, Pruesse E, Yilmaz P, Gerken J, Schweer T, Yarza P, et al. The silva ribosomal rna gene database project: improved data processing and web-based tools. Nucleic Acids Res. 2012;41:D590–6.
38. Oksanen J, Simpson G, Blanchet F, R K, P L, P M, et al. Vegan: Community Ecology Package-r package version 2.6–6.1. 2024.
39. Jiao S, Lu Y. Abundant fungi adapt to broader environmental gradients than rare fungi in agricultural fields. Glob Chang Biol. 2020;26:4506–20.
40. Wemheuer F, Taylor JA, Daniel R, Johnston E, Meinicke P, Thomas T, et al. Tax4Fun2: prediction of habitat-specific functional profiles and functional redundancy based on 16s rrna gene sequences. Environ Microbiome. 2020;15:11.
41. Newman ME. The structure and function of complex networks. SIAM Rev. 2003;45:167–256.
42. Newman ME. Modularity and community structure in networks. Proc Natl Acad Sci USA. 2006;103:8577–82.
43. Bastian M, Heymann S, Jacomy M. Gephi: an open source software for exploring and manipulating networks. ICWSM Conf. 2009;8:361–2.
44. Kembel SW, Cowan PD, Helmus MR, Cornwell WK, Morlon H, Ackerly DD, et al. Picante: R tools for integrating phylogenies and ecology. Bioinformatics. 2010;26:1463–4.
45. Chen W, Ren K, Isabwe A, Chen H, Liu M, Yang J. Stochastic processes shape microeukaryotic community assembly in a subtropical river across wet and dry seasons. Microbiome. 2019;7:1–16.
46. Sloan WT, Woodcock S, Lunn M, Head IM, Curtis TP. Modeling taxa-abundance distributions in microbial communities using environmental sequence data. Microb Ecol. 2007;53:443–55.
47. Levins R. Evolution in changing environments: some theoretical explorations: Princeton University Press, 1968.
48. Salazar G. EcolUtils: utilities for community ecology analysis. R package version. 2020;3.
49. Wu W, Logares R, Huang B, Hsieh C-H. Abundant and rare picoeukaryotic sub-communities present contrasting patterns in the epipelagic waters of marginal seas in the northwestern pacific ocean. Environ Microbiol. 2017;19:287–300.
50. Zhou J, Wu L, Deng Y, Zhi X, Jiang Y-H, Tu Q, et al. Reproducibility and quantitation of amplicon sequencing-based detection. ISME J. 2011;5:1303–13.

Publisher's Note